Free
eBook
download

Glasses and Glass Ceramics

Current state of research in the synthesis, modification, and characterization

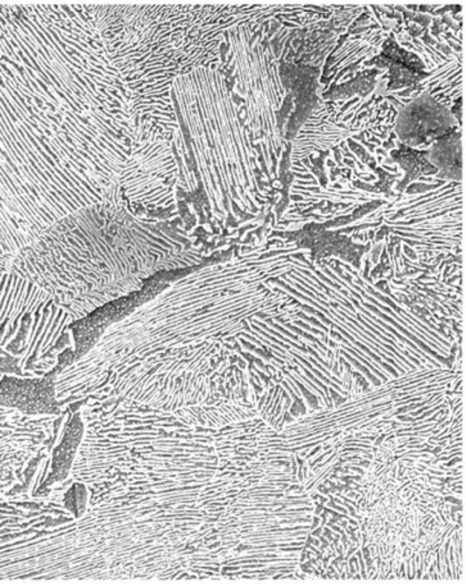

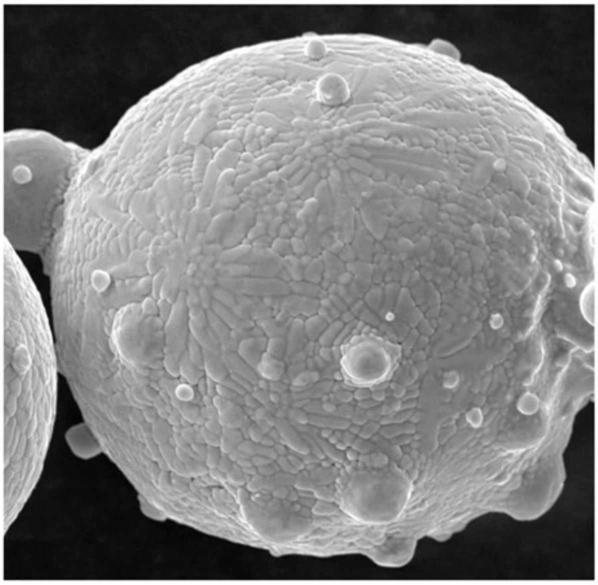

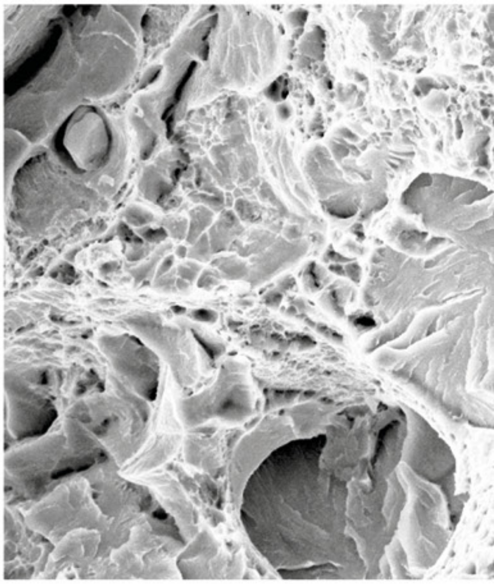

WILEY

POLYTECH
Peter the Great
St.Petersburg Polytechnic
University

ADVANCED MATERIALS
www.advmat.de

Are Cu_2Te-Based Compounds Excellent Thermoelectric Materials?

Kunpeng Zhao, Ke Liu, Zhongmou Yue, Yancheng Wang, Qingfeng Song, Jian Li, Mengjia Guan, Qing Xu, Pengfei Qiu, Hong Zhu, Lidong Chen,* and Xun Shi**

Most of the state-of-the-art thermoelectric (TE) materials exhibit high crystal symmetry, multiple valleys near the Fermi level, heavy constituent elements with small electronegativity differences, or complex crystal structure. Typically, such general features have been well observed in those well-known TE materials such as Bi_2X_3-, SnX-, and PbX-based compounds (X = S, Se, and Te). The performance is usually high in the materials with heavy constituent elements such as Te and Se, but it is low for light constituent elements such as S. However, there is a great abnormality in Cu_2X-based compounds in which Cu_2Te has much lower TE figure of merit (zT) than Cu_2S and Cu_2Se. It is demonstrated that the Cu_2Te-based compounds are also excellent TE materials if Cu deficiency is sufficiently suppressed. By introducing Ag_2Te into Cu_2Te, the carrier concentration is substantially reduced to significantly improve the zT with a record-high value of 1.8, 323% improvement over Cu_2Te and outperforms any other Cu_2Te-based materials. The single parabolic band model is used to further prove that all Cu_2X-based compounds are excellent TE materials. Such finding makes Cu_2X-based compounds the only type of material composed of three sequent main group elements that all possess very high zTs above 1.5.

With the increasingly serious environmental pollution and intensified energy crisis, exploitation and utilization of new kinds of clean energy resources are imperative. Among them, thermoelectric (TE) conversion technology based on high-performance TE materials enables direct energy conversion between heat and electricity through the movement of internal phonons and charge carriers.[1–4] It has shown extensive and important prospects in power generation using industrial waste heat and electronic refrigeration.[5] The energy conversion efficiency of a TE material is mainly determined by its dimensionless figure of merit, defined as $zT = \sigma S^2 T/(\kappa_L + \kappa_e)$, where σ, S, T, κ_L, and κ_e are the electrical conductivity, Seebeck coefficient, absolute temperature, lattice thermal conductivity, and electronic thermal conductivity, respectively. The general criteria for high zTs require high crystal symmetry for materials, many valleys (carrier pockets) near the Fermi level, heavy elements with small electronegativity differences between the constituent elements, or complex crystal structure, etc.[6–10] For the constituent elements in the same group such as S, Se, and Te, the heavy one (Te and Se) always has large atomic mass for low κ_L and more covalent bonding character for large carrier mobility (μ_H) and thus outstanding electrical transports.[10] Therefore, the zTs are usually high in tellurides and selenides, but they are low in sulfides. This is the general phenomenon that has been observed in those well-known TE materials such as Bi_2X_3-, SnX-, and PbX-based compounds (X = S, Se, and Te).[11–47] As shown in **Figure 1**, the zT values gradually improve as the anion element change from S to Se and then to Te. However, the case is different in Cu_2X-based liquid-like TE materials that are among the hottest materials in recent TE study. They possess exceptionally low thermal conductivity and excellent zTs with the values of 1.7–1.9 for Cu_2S, 1.5–2.3 for Cu_2Se, and 0.4–1.1 for Cu_2Te (see Figure 1).[48–62] It is quite abnormal and interesting that the zT in Cu_2Te is lower than those in Cu_2S and Cu_2Se. As we known, tellurium is less electronegative, thus the chemical bonds between Cu and Te should be less ionic as compared with those in Cu_2S and Cu_2Se, which is beneficial for large μ_H and electrical transports. Besides, the κ_L in Cu_2Te is expected lower than or similar to those in Cu_2S and Cu_2Se because tellurium is much heavier than sulfur and

Dr. K. Zhao, Prof. X. Shi
State Key Laboratory of Metal Matrix Composites
School of Materials Science and Engineering
Shanghai Jiao Tong University
Shanghai 200240, China
E-mail: xshi@sjtu.edu.cn

K. Liu, Prof. H. Zhu
University of Michigan-Shanghai Jiao Tong University Joint Institute
Shanghai Jiao Tong University
Shanghai 200240, China

Z. Yue, Y. Wang, Q. Song, J. Li, M. Guan, Q. Xu, Prof. P. Qiu,
Prof. L. Chen, Prof. X. Shi
State Key Laboratory of High Performance Ceramics and Superfine Microstructure
Shanghai Institute of Ceramics
Chinese Academy of Sciences
Shanghai 200050, China
E-mail: qiupf@mail.sic.ac.cn; cld@mail.sic.ac.cn

Z. Yue, Y. Wang, Q. Song, J. Li, M. Guan, Q. Xu, Prof. L. Chen,
Prof. X. Shi
Center of Materials Science and Optoelectronics Engineering
University of Chinese Academy of Sciences
Beijing 100049, China

The ORCID identification number(s) for the author(s) of this article can be found under https://doi.org/10.1002/adma.201903480.

DOI: 10.1002/adma.201903480

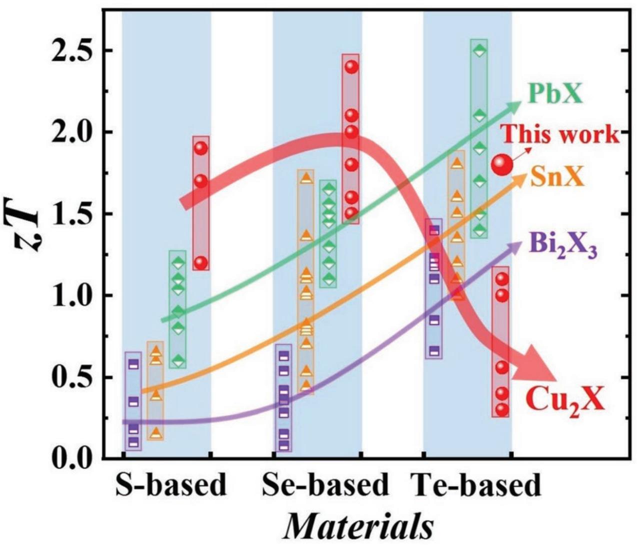

Figure 1. Reported zT values of polycrystalline PbX-, SnX-, Bi_2X_3-, and Cu_2X-based (X = S, Se, and Te) TE materials. The red sphere symbol represents the data of Cu_2Te in this study. The other data are taken from refs. [11–62].

selenium. These two features definitely make Cu_2Te potentially high zTs superior to Cu_2S and Cu_2Se. The deep analysis shows that such abnormality is mainly ascribed to two aspects. On the one hand, the hole concentration (p_H) of Cu_2Te is too high (>10^{21} cm^{-3}) owing to its severe copper deficiency.[60] On the other hand, Cu_2Te has too complex phase diagram to control material's quality, especially it has at least five phase transitions from its melting point to room temperature.[63] Although a few strategies have been used to tune the lattice defects and TE properties of Cu_2Te, the current maximum zT is only around 1.1,[60] which is much smaller than those in Cu_2S and Cu_2Se. This is in contradiction with the general trend observed in other typical TE materials (see Figure 1). Furthermore, this leaves the open questions what is the true zT in Cu_2Te and are Cu_2Te-based compounds excellent TE materials? In this study, we demonstrate that the zT in Cu_2Te-based compounds can be as high as 1.8 (Figure 1). Same as Cu_2S and Cu_2Se, they are excellent TE materials when their lattice defects and phase transition features are well tuned and optimized.

Cu_2Te has too large hole concentrations (p_H) due to the presence of large amount of intrinsic Cu deficiency. Improving Cu amount can lower the Cu deficiency within a certain range but such reduction is very limited. Previous study showed that the vacancy formation energies of Ag_2Te are gradually decreased after the substitution of Cu at Ag sites.[64] As a result, the carrier concentration of $Ag_{2-x}Cu_xTe$ is gradually increased upon increasing the Cu contents. Since Ag_2Te has the similar cubic structure as Cu_2Te at high temperature, we thus expect the carrier concentration of Cu_2Te can be reduced by alloying Ag at Cu sites. Thus, herein we try to choose Ag to replace Cu to balance the Cu deficiency. The room temperature X-ray diffraction (XRD) patterns measured on powder Cu_2Te + x% Ag_2Te (x = 0, 15, 35, 40, 50, and 55) are depicted in **Figure 2**a. The phase compositions of pristine Cu_2Te are very complicated according to the literatures.[60] Our XRD data show that it consists of multiple phases, including hexagonal, monoclinic, and orthorhombic phases (Figure S1, Supporting Information). After introducing Ag_2Te into Cu_2Te, some new diffraction peaks appear in the XRD patterns, which are mainly indexed to the hexagonal CuAgTe phase. These data show that it is inclined to form secondary phase rather than forming solid-solutions at room temperature for Cu_2Te + x% Ag_2Te. Similar phenomenon was also observed in Cu_2Se-Ag_2Se and Cu_2S-Ag_2S systems.[59,65] However, pure phase is observed after going through the phase transitions at high temperatures. As demonstrated in Figure 2b, nearly all the diffraction peaks at 900 K can be indexed to the Cu_2Te cubic structure (PDF#053116) with the space group of $F\bar{4}3m$. This suggests that all the samples transform into single cubic phase at high temperatures and the second phase at room temperature dissolve into the matrix after the final structural transition. Besides, the diffraction peaks are shifted to a lower angle upon increasing the Ag_2Te content, indicating that the lattice constants increase with the increase of Ag_2Te content.

Figure 2c plots the measured differential scanning calorimetry (DSC) curves for Cu_2Te + x% Ag_2Te (x = 0, 15, 35, 50, and 55). For Cu_2Te, five successive phase transitions are observed with the transition temperatures somewhat different from the literatures due to its complex phase compositions. The number and temperature of phase transition, and peak intensity of DSC curves are all changed when adding Ag into Cu_2Te. Specifically, the temperature of the last phase transition between hexagonal phase and cubic phase is weakened and lowered from 815 K in Cu_2Te to 720 K in Cu_2Te + 15% Ag_2Te, and finally disappears in Cu_2Te + 55% Ag_2Te (see Figure 2d). This is also consistent with that Ag is dissolved into the Cu_2Te matrix with increasing the temperature. Such reduced phase transition temperature T_c is mainly attributed to the decreased ratio of the enthalpy change ΔH to the entropy change ΔS.

Figure 3 displays the temperature dependence of TE properties for Cu_2Te + x% Ag_2Te (x = 0, 15, 35, 40, 50, and 55). When x is less than 50, the electrical conductivity σ decreases in the entire temperature range as the content of Ag_2Te increases. Specifically, the room temperature σ decreases significantly from 4.2×10^5 S m^{-1} for Cu_2Te to 1.0×10^5 S m^{-1} for Cu_2Te + 50% Ag_2Te. The reverse trend at around $x = 55$ may be related to the decreased band gap E_g since CuAgTe has a much lower E_g than that of Cu_2Te.[64] As the temperature increases, the electrical conductivity is roughly decreased except for the phase transition regions, behaving as a highly degenerate semiconductor. In contrast, the Seebeck coefficient S of Cu_2Te + x% Ag_2Te is roughly increased with increasing temperature. At room temperature, S is scarcely changed or even decreased when the Ag_2Te content is larger than 15%. The reason for this should be that Cu_2Te is a p-type semiconductor while CuAgTe is an n-type semiconductor at room temperature,[64] thus the total Seebeck coefficients are partly counterbalanced. However, at high temperatures, all the samples have single cubic phases with one dominant type of carriers, i.e., holes. Therefore, the Seebeck coefficient increases significantly with increasing the Ag_2Te content. The increased Seebeck coefficient coupled with the decreased electrical conductivity implies that the hole concentration is reduced at high temperatures. We have tried to corroborate our speculation by measuring the carrier concentrations at different temperature. Unfortunately, no reliable data are obtained at high temperature.

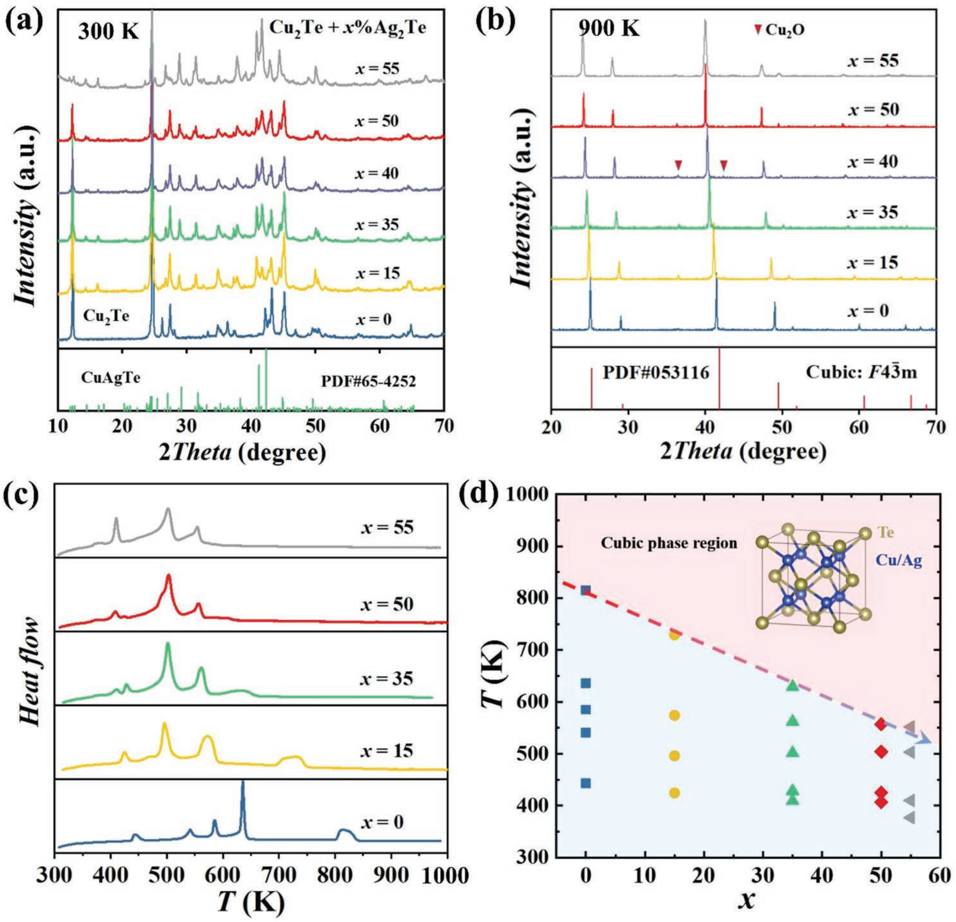

Figure 2. PXRD for $Cu_2Te + x\%\ Ag_2Te$ (x = 0, 15, 35, 40, 50, and 55) at a) 300 K and b) 900 K. Some weak reflections belong to Cu_2O are marked with red triangles. The oxidation of $Cu_2Te + x\%\ Ag_2Te$ during the processes of fabrication or measurement should be avoided considering the poor TE performance of Cu_2O.[66,67] c) DSC curves measured from 310 to 1000 K. d) Phase transition temperature T_c as a function of Ag_2Te content. The inset illustrates the cubic crystal structure of Cu_2Te.

We thus performed defect formation energy (E_{form}) calculations by using the high temperature cubic structures for Cu_2Te and CuAgTe (see Figure S3, Supporting Information). The E_{form} values for Cu vacancy (V_{Cu}) or/and Ag vacancy (V_{Ag}) are calculated according to the equation

$$E_{\text{form}} = E_{\text{tot}}\,[\text{defected}] - E_{\text{tot}}\,[\text{perfect}] + \sum_{i} n_i \mu_i + qE_f + E_{\text{corr}} \quad (1)$$

where E_{tot}[defected] and E_{tot}[perfect] are the total energy of defected and perfect structures, respectively; $\sum_i n_i\mu_i$ is the summation over the atomic chemical potentials; q is the charge of defect; E_f is the fermi energy; and E_{corr} is the correction due to spurious electrostatic interaction of charged cell in periodic boundary calculation. The generalized gradient approximation (GGA) level band gap is zero for Cu_2Te and CuAgTe, leading to negligible E_{corr}. The atomic chemical potentials were calculated from the ternary phase diagram for Cu-Ag-Te, constructed by using the Pymatgen code based on density functional theory ground state energies from the Materials Project database.[68,69] The calculation results based on the 2 × 2 × 2 supercell are shown in **Figure 4**. The slanting lines with negative slope represent the defect formation energies for negatively charged V_{Cu} and V_{Ag} defects. The Cu vacancy formation energy in Cu_2Te is very low, suggesting that V_{Cu} defects are prone to be formed during the fabrication processes. Thus, severe copper precipitation and quite high hole carrier concentration are expected in Cu_2Te, which is consistent with the experiment observation. The carrier concentration of Cu_2Te should be scarcely changed from room temperature to high temperatures although it experiences complex phase transitions. With the addition of Ag, the V_{Cu} formation energy is increased within all the Fermi level range, implying that the formation of V_{Cu} is suppressed. Besides, we also take into account the possible formation of V_{Ag}, whose formation energy is higher than that of Cu vacancy (see Figure 4). This indicates that V_{Ag} is more difficult to be created in CuAgTe as compared with V_{Cu}. Furthermore, the convergence tests of the size effects on defect formation energies have been also performed for Cu_2Te and CuAgTe. Three different supercells, i.e., 1 × 1 × 1, 2 × 2 × 2, and 3 × 3 × 3 were tested. As shown in Figure S4 in the Supporting Information, the calculated energies between the 2 × 2 × 2 and 3 × 3 × 3 supercells are very close. The trends for energy variation of Cu vacancy or Ag vacancy in different supercells are also the same. Therefore, the substitution of Ag for Cu can decrease

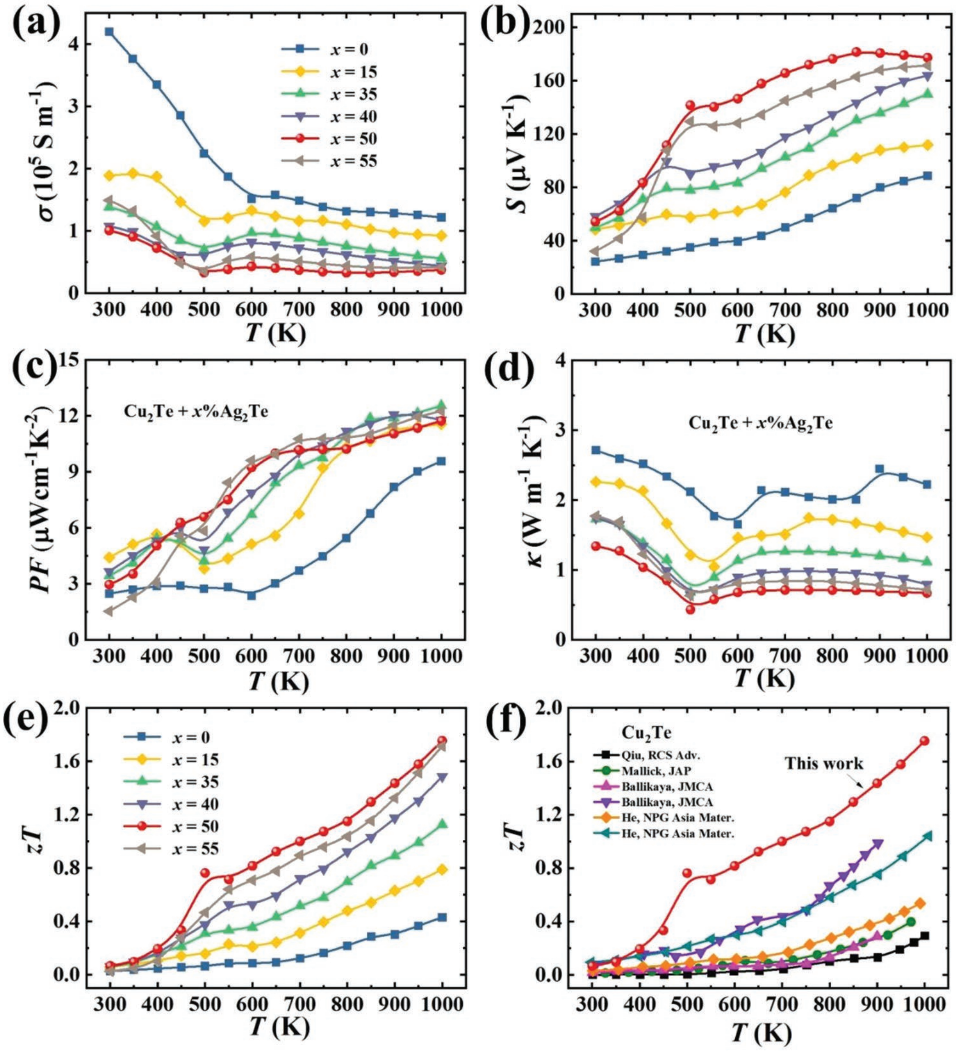

Figure 3. Temperature dependence of TE properties for Cu_2Te + *x*% Ag_2Te (*x* = 0, 15, 35, 40, 50, and 55). a) Electrical conductivity σ, b) Seebeck coefficient *S*, c) power factor PF, d) total thermal conductivity κ, and e) TE figure of merit *zT*. f) Comparison of *zT* values from 300 to 1000 K for several reported Cu_2Te-based TE materials.[59–62]

the formation of cation vacancies, resulting in much lower hole concentrations.

The power factors calculated from the formula PFs = $S^2\sigma$ are shown in Figure 3c. The PF for pristine Cu_2Te is around 2.8 μW cm^{-1} K^{-2} below 600 K and subsequently increases with increasing temperature. A maximum PF of 9.5 μW cm^{-1} K^{-2} is obtained at 1000 K for Cu_2Te. After introducing Ag_2Te into Cu_2Te, the PFs increase in the entire temperature range except for Cu_2Te + 55% Ag_2Te, which shows a low PF near room temperature because of the influence of minor carriers (i.e., electrons). Nevertheless, in the middle temperature range, the PFs are greatly improved due to the suppression of phase transition temperature and the reduction of hole concentration. For instance, a high PF value of 9 μW cm^{-1} K^{-2} is achieved at 600 K for Cu_2Te + 50% Ag_2Te, which is five times higher than that for pristine Cu_2Te at the same temperature.

Figure 3d displays the total thermal conductivity κ as a function of temperature for Cu_2Te + *x*% Ag_2Te (*x* = 0, 15, 35, 40, 50, and 55). They show complicated temperature dependencies in the temperature range from 300 to 1000 K due to the existence of multiple phase transitions. The κ is significantly decreased with increasing Ag_2Te content, which is mainly attributed to the decreased contribution of charge carriers to thermal transport. The lattice thermal conductivity κ_L for Cu_2Te + *x*% Ag_2Te is calculated and shown in Figure S5 in the Supporting Information. All the samples exhibit ultralow lattice thermal conductivity κ_L with the values around 0.3 W m^{-1} K^{-1} at 900 K, which is even lower than the minimum lattice thermal conductivity (κ_{min}) estimated by Cahill's model (see the details in the Supporting Information).[70]

Figure 3e presents the temperature dependence of *zT* for Cu_2Te + *x*% Ag_2Te (*x* = 0, 15, 35, 40, 50, and 55). At low temperature, both holes and electrons are involved in transport, resulting in relatively low *zT* values. However, at high temperature, the TE performance is greatly improved over a large temperature range, which can be traced to the suppressed phase

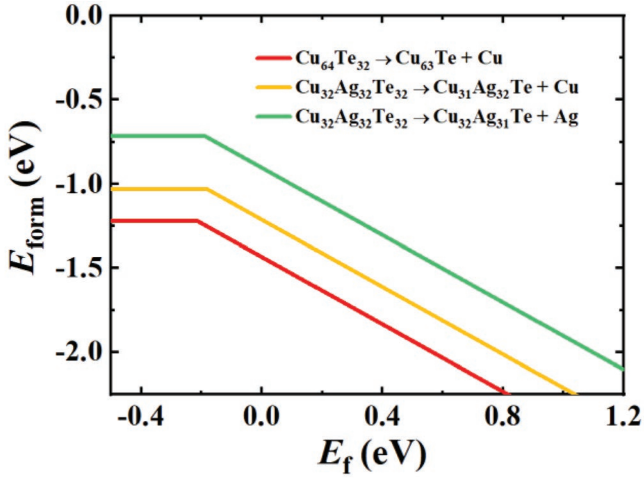

Figure 4. Calculated defect formation energy E_{form} for copper/silver vacancy in Cu_2Te and CuAgTe as a function of Fermi energy. A 2 × 2 × 2 supercell containing 96 atoms, i.e., $Cu_{64}Te_{32}$ or $Cu_{32}Ag_{32}Te_{32}$, is constructed for calculations. Zero Fermi energy is with respect to the valence band maximum for respective compounds.

transition temperature and the reduced carrier concentration. Specifically, the maximum zT value for pristine Cu_2Te is only 0.4 and it is remarkably boosted to 1.8 for Cu_2Te + 50% Ag_2Te at 1000 K. This is a 323% improvement over Cu_2Te itself and outperforms any other Cu_2Te-based material reported so far (Figure 3f).[59–62]

To further elucidate on the high TE performance of Cu_2Te, we modeled their TE properties using a single parabolic band (SPB) model with the carrier mobility limited by acoustic phonon scattering.[44,51] In comparison, the data of Cu_2S and Cu_2Se are also modeled. The experimental data at 900 K are selected because all materials have same cubic structures at this temperature. Thus, the effect of different crystal structures on TE properties can be excluded. The model details are shown in the Supporting Information. Because the Hall data at 900 K is absent, we do not have the exact drift mobility μ_0 or effective mass m^*. However, we can fit the S–σ (Seebeck coefficient vs electrical conductivity) curves by taking the weighted mobility ($\mu_0 m^{*3/2}$) as a single parameter (see Equation (S6), Supporting Information). As shown in **Figure 5**a, the red dashed line is calculated by using a weighted mobility $\mu_0 m^{*3/2}$ of 19.6 $m_e^{3/2}$ cm^2 V^{-1} s^{-1}. All the experimental S data for three different types of materials fall around on this derived line. This strongly suggests that Cu_2Te-, Cu_2Se-, and Cu_2S-based compounds have comparable weighted mobility parameter $\mu_0 m^{*3/2}$ at high temperature. Thus, Cu_2Te-, Cu_2Se-, and Cu_2S-based compounds may have similar good electrical transport properties, which is further supported by the calculated power factors (see Figure 5b). All the data for Cu_2S, Cu_2Se, and Cu_2Te show a very nice agreement with the calculated curve. The only difference among Cu_2S, Cu_2Se, and Cu_2Te is the position of Fermi level. It is near the top of valence band for Cu_2S, in the deep covalent band for Cu_2Te, and in the middle for Cu_2Se. Thus, the electrical conductivity is low in Cu_2S, in the middle in Cu_2Se, and very high in Cu_2Te. According to Figure 5b,

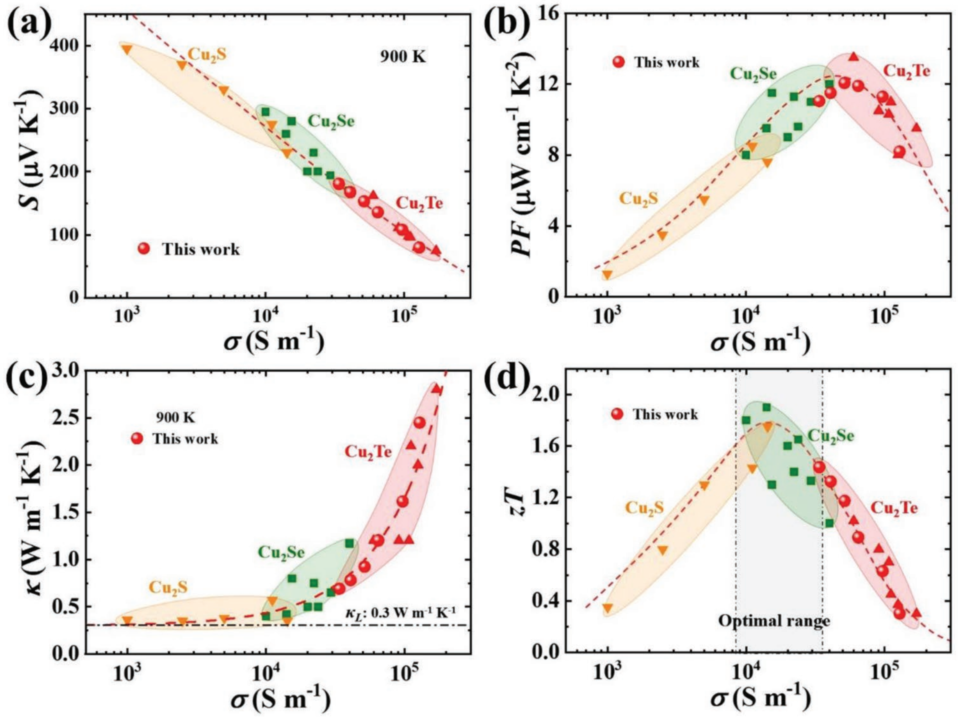

Figure 5. Comparison of TE properties among Cu_2Te, Cu_2Se, and Cu_2S-based materials at 900 K. a) Seebeck coefficient S, b) power factor PF, c) total thermal conductivity κ, and d) zT values as a function of electrical conductivity σ. The red circle symbols are experimental data in this work. The other symbols are the data from refs. [48–62]. The dashed lines are derived from the single parabolic band (SPB) model with the weighted mobility $\mu_0 m^{*3/2}$ of 19.6 $m_e^{3/2}$ cm^2 V^{-1} s^{-1}.

the optimal electrical conductivity σ_{opt} for maximized PF is around 5×10^4 S m^{-1}, which can be easily achieved in Cu_2Se. Due to the severe copper deficiency, Cu_2Te-based compounds have quite high electrical conductivity ($\approx 10^5$ S m^{-1}) that greatly exceeds the σ_{opt} value. Thus, its PF is relatively low. On the contrary, Cu_2S-based compound has very low electrical conductivity ($\approx 10^3$ S m^{-1}) that is much less than the σ_{opt} value, thus its PF is also very low. The electrical conductivity for Cu_2Se-based compound lies between that of Cu_2Te and Cu_2S. Nevertheless, according to our analysis, the PFs for all the Cu_2X compounds can be tuned to the optimal range when their electrical conductivity and carrier concentration are optimized.

The κ–σ (total thermal conductivity vs electrical conductivity) relation is calculated under the assumption that κ_L is 0.3 W m^{-1} K^{-1} for all materials. This is an acceptable assumption for these liquid-like materials with ultralow lattice thermal conductivity. As plotted in Figure 5c, the experimental data agree well with the calculated curve, indicating that the total thermal conductivity is dominated by carrier thermal conductivity in Cu_2X-based compounds. When increasing electrical conductivity, the total thermal conductivity is greatly improved. Thus, Cu_2S-based compounds generally have very low κ, whereas Cu_2Te-based compounds have quite high κ.

The zT value as a function of σ is then calculated based on the PF and κ derived above, which is plotted in Figure 5d. The optimal electrical conductivity range for the maximized zT is around (1–3) $\times 10^4$ S m^{-1}, which is slightly lower than that for PF because of the contribution from electronic thermal conductivity. Apparently, the electrical conductivity for Cu_2Se is close to the optimal value, thus high zT's are easily achieved in Cu_2Se. Whereas the σ values in Cu_2S and Cu_2Te are either less or larger than the optimal value, resulting in low zT values. Increasing the σ in Cu_2S and decreasing the σ in Cu_2Te can approach the optimal range for high zTs. In this study, when adding Ag into Cu_2Te, the σ is greatly reduced and its TE performance is significantly improved. The above data and analysis clearly demonstrate that Cu_2Te is also an excellent TE material. It is not against the general trend shown in Figure 1. Furthermore, due to the ultralow κ_L in these liquid-like materials, all Cu_2S, Cu_2Se, and Cu_2Te possess very high zTs when their electrical properties are optimized. This is beyond the other TE materials. Currently, it is the only material system that possesses very high zTs above 1.5 in the materials with all three constituent elements in the same group such as S, Se, and Te.

While Cu_2X-based liquid-like compounds are promising TE materials with high zT values, the migration of Cu ions causes long-term stability problems under electric field and/or temperature gradient.[71–74] Such stability issue has been well studied recently, which is determined by the critical voltage of Cu ions.[73] Even Cu/Ag moves fast, the liquid-like materials can still be stable if the critical voltage is large enough.[73,74] The critical voltage for Cu_2X-based materials is around 0.1 V, which is a few orders of higher than the voltage (0.0001 V) used for TE property measurements. To validate the sample stability under small voltage/current, repeatability measurements are performed on Cu_2Te + 35% Ag_2Te for six cycles with different cycling temperatures. As presented in Figure S6 in the Supporting Information, both the σ and S show quite good reproducibility up to 1000 K with just a little change below the phase transition temperatures (<500 K) because of the presence of mixed phases.

To sum up, by introducing Ag_2Te into Cu_2Te, the high carrier concentration in pristine Cu_2Te is substantially reduced to an optimal range, resulting in much reduced thermal conductivity and enhanced power factors over the entire temperature range. Furthermore, the temperature of last phase transition is significantly lowered when increasing Ag content, which benefits to maintain the good TE properties of cubic phase at low temperatures. A maximum zT of 1.8 is achieved at 1000 K in Cu_2Te + 50% Ag_2Te, which is the highest reported value for Cu_2Te-based TE materials. An effective SPB model was used to model the transport properties of Cu_2S-, Cu_2Se-, and Cu_2Te-based compounds and it was found that they are all outstanding TE materials. This conclusion is beyond the general trend observed in other TE materials in which very high zTs cannot be achieved in all the sulfides, selenides, and tellurides.

Experimental Section

Synthesis: A series of samples with nominal compositions of Cu_2Te + x% Ag_2Te (x = 0, 15, 35, 40, 50, and 55) was synthesized by vacuum melting combined with the spark plasma sintering (SPS) process. High purity Cu (Sigma Aldrich, 99.999%), Ag (Sigma Aldrich, 99.999%), and Te (Sigma Aldrich, 99.999%) were weighed out and loaded into boron nitride crucibles that were sealed in a fused silica tube under vacuum. The loaded tubes were slowly heated to 1403 K in 12 h and soaked at this temperature for 6–12 h, then rapidly quenched to room temperature in water. Next, the sealed tubes were heated to 973 K in 8 h, dwelled at this temperature for 6 days, and subsequently cooled to room temperature by turning off the furnace power. The obtained ingots were hand-ground into fine powders using a mortar and a pestle. Then the powders were loaded into a graphite die with a diameter of 10 mm and then consolidated via SPS (Sumitomo SPS-2040) at 773–873 K under a pressure of 50–60 MPa for 5 min. Electrically insulating but thermally conducting boron nitride layers were coated on the carbon foils and the inner sides of the graphite died before the SPS process. Highly dense (>98% of theoretical density) disk-shaped pellets with dimensions of 10 mm in diameter and about 5 mm in thickness were obtained.

Characterization: Room-temperature powder X-ray diffraction (RT-PXRD) analysis was performed on Rigaku Rint 2000 with a Cu-K$_\alpha$ source. High-temperature PXRD patterns were collected at 900 K on a powder X-ray diffractometer (Bruker D8 Advance) with high temperature accessory operating at 45 kV and 200 mA. The sample compositions were measured by field emission scanning electron microscopy (Magellan-400) equipped with energy dispersive X-ray analysis (Horiba 250). The sound speed data were obtained by an ultrasonic measurement system UMS-100 with shear wave transducers of 5 MHz and longitudinal wave transducers of 10 MHz. DSC measurement was carried out using a Netzsch DSC 404FE instrument. The electrical conductivity (σ) and Seebeck coefficient (S) were measured simultaneously in a helium atmosphere using a commercial apparatus (ULVAC ZEM-3). Thermal diffusivity (D) was measured via the laser flash method using a Netzsch LFA-457. The pellet density (d) was measured by the Archimedes method. The C_p for Cu_2Te + 55% Ag_2Te sample was measured by using the commercial DSC equipment (see Figure S7, Supporting Information). The total thermal conductivity was calculated via the equation $\kappa = d \times C_p \times D$. The measurement errors for the electrical conductivity, the Seebeck coefficient, and the thermal conductivity were 5%, 7%, and 5%, respectively.

Defect Formation Energy Calculation: The present calculations were performed using the Perdew–Burke–Ernzerhof-GGA[75,76] with projector-augmented wave method,[77] as implemented in the Vienna Ab Initio

Simulation Package (VASP).[78] The high temperature cubic structures for Cu_2Te and CuAgTe with ordered Cu and Ag distribution were adopted for all the calculations (see Figure S3, Supporting Information). Besides, a special quasi-random structure for CuAgTe to mimic a random distribution of Cu and Ag was also adopted based on "mcsqs" code of the Alloy Theoretic Automated Toolkit (ATAT).[79] The obtained defect formation energy in the special quasi-random structure was close to that in the ordered structure (see Figure S8, Supporting Information). For simplicity, only the 8c sites were taken into account since the 32f site occupation would make the Cu_2Te/CuAgTe less stable at 0 K. Three different crystal cells, i.e., $1 \times 1 \times 1$, $2 \times 2 \times 2$, and $3 \times 3 \times 3$ supercells with $6 \times 6 \times 6$, $3 \times 3 \times 3$, and $2 \times 2 \times 2$ gamma centered k-point meshes, respectively, were employed for numerical integrations over the Brillouin zone. A fixed constant occupancy of the defects state was used in calculations. The cutoff energy of the plane wave was set at 520 eV. The energy convergence criterion was chosen to be 5.0×10^{-3} eV per unit cell. It should be noted that the calculated energy in this study might have large uncertainties (such as the negative formation energies), but the relative value was quoteworthy and the conclusions were reasonable.

Supporting Information

Supporting Information is available from the Wiley Online Library or from the author.

Acknowledgements

The authors thank Prof. Yiyang Sun of Shanghai Institute of Ceramics for helpful discussions. This work was financially supported by the National Key Research and Development Program of China (2018YFB0703600), National Natural Science Foundation of China (nos. 51625205 and 51961135106), Key Research Program of Chinese Academy of Sciences (grant no. KFZD-SW-421). P.Q. thanks for the support by the Youth Innovation Promotion Association of CAS under grant no. 2016232.

Conflict of Interest

The authors declare no conflict of interest.

Keywords

electrical transport, single parabolic bands, telluride, thermal conductivity, thermoelectric materials

Received: May 31, 2019
Revised: September 13, 2019

---

[1] X. Shi, L. Chen, C. Uher, *Int. Mater. Rev.* **2016**, *61*, 379.
[2] W. G. Zeier, A. Zevalkink, Z. M. Gibbs, G. Hautier, M. G. Kanatzidis, G. J. Snyder, *Angew. Chem., Int. Ed.* **2016**, *55*, 6826.
[3] G. Tan, L. D. Zhao, M. G. Kanatzidis, *Chem. Rev.* **2016**, *116*, 12123.
[4] T. Zhu, Y. Liu, C. Fu, J. P. Heremans, J. G. Snyder, X. Zhao, *Adv. Mater.* **2017**, *29*, 1605884.
[5] X. Shi, L. Chen, *Nat. Mater.* **2016**, *15*, 691.
[6] Y. Pei, X. Shi, A. LaLonde, H. Wang, L. Chen, G. J. Snyder, *Nature* **2011**, *473*, 66.
[7] J. Zhang, R. Liu, N. Cheng, Y. Zhang, J. Yang, C. Uher, X. Shi, L. Chen, W. Zhang, *Adv. Mater.* **2014**, *26*, 3848.
[8] J. Li, X. Zhang, Z. Chen, S. Lin, W. Li, J. Shen, I. T. Witting, A. Faghaninia, Y. Chen, A. Jain, *Joule* **2018**, *2*, 976.
[9] G. J. Snyder, E. S. Toberer, *Nat. Mater.* **2008**, *7*, 105.
[10] G. A. Slack, in *Handbook of Thermoelectrics* (Ed: D. Rowe), CRC, Boca Raton, FL **1995**, pp. 407–440.
[11] W. Liu, K. C. Lukas, K. McEnaney, S. Lee, Q. Zhang, C. P. Opeil, G. Chen, Z. Ren, *Energy Environ. Sci.* **2013**, *6*, 552.
[12] Z. H. Ge, P. Qin, D. He, X. Chong, D. Feng, Y. H. Ji, J. Feng, J. He, *ACS Appl. Mater. Interfaces* **2017**, *9*, 4828.
[13] Y. Kawamoto, H. Iwasaki, *J. Electron. Mater.* **2014**, *43*, 1475.
[14] G. L. Sun, L. L. Li, X. Y. Qin, D. Li, T. H. Zou, H. X. Xin, B. J. Ren, J. Zhang, Y. Y. Li, X. J. Li, *Appl. Phys. Lett.* **2015**, *106*, 053102.
[15] G. Sun, X. Qin, D. Li, J. Zhang, B. Ren, T. Zou, H. Xin, S. B. Paschen, X. Yan, *J. Alloys Compd.* **2015**, *639*, 9.
[16] F. Hao, P. Qiu, Y. Tang, S. Bai, T. Xing, H.-S. Chu, Q. Zhang, P. Lu, T. Zhang, D. Ren, J. Chen, X. Shi, L. Chen, *Energy Environ. Sci.* **2016**, *9*, 3120.
[17] B. Poudel, Q. Hao, Y. Ma, Y. Lan, A. Minnich, B. Yu, X. Yan, D. Wang, A. Muto, D. Vashaee, *Science* **2008**, *320*, 634.
[18] Y. Pan, Y. Qiu, I. Witting, L. Zhang, C. Fu, J.-W. Li, Y. Huang, F.-H. Sun, J. He, G. J. Snyder, C. Felser, J.-F. Li, *Energy Environ. Sci.* **2019**, *12*, 624.
[19] B. Xu, T. Feng, M. T. Agne, L. Zhou, X. Ruan, G. J. Snyder, Y. Wu, *Angew. Chem., Int. Ed.* **2017**, *56*, 3546.
[20] Y. Pan, U. Aydemir, J. A. Grovogui, I. T. Witting, R. Hanus, Y. Xu, J. Wu, C. F. Wu, F. H. Sun, H. L. Zhuang, *Adv. Mater.* **2018**, *30*, 1802016.
[21] B. Zhou, S. Li, W. Li, J. Li, X. Zhang, S. Lin, Z. Chen, Y. Pei, *ACS Appl. Mater. Interfaces* **2017**, *9*, 34033.
[22] Q. Tan, L.-D. Zhao, J.-F. Li, C.-F. Wu, T.-R. Wei, Z.-B. Xing, M. G. Kanatzidis, *J. Mater. Chem. A* **2014**, *2*, 17302.
[23] Z.-G. Chen, X. Shi, L.-D. Zhao, J. Zou, *Prog. Mater. Sci.* **2018**, *97*, 283.
[24] Y. Li, X. Shi, D. Ren, J. Chen, L. Chen, *Energies* **2015**, *8*, 6275.
[25] Q. Zhang, E. K. Chere, J. Sun, F. Cao, K. Dahal, S. Chen, G. Chen, Z. Ren, *Adv. Energy Mater.* **2015**, *5*, 1500360.
[26] Y. Luo, J. Yang, Q. Jiang, W. Li, D. Zhang, Z. Zhou, Y. Cheng, Y. Ren, X. He, *Adv. Energy Mater.* **2016**, *6*, 1600007.
[27] Y. K. Lee, K. Ahn, J. Cha, C. Zhou, H. S. Kim, G. Choi, S. I. Chae, J. H. Park, Y. Lee, C. H. Park, S. P. Cho, S. H. Park, Y. E. Sung, W. B. Lee, T. Hyeon, I. Chung, *J. Am. Chem. Soc.* **2017**, *139*, 10887.
[28] X. Shi, K. Zheng, M. Hong, W. Liu, R. Moshwan, Y. Wang, X. Qu, Z. G. Chen, J. Zou, *Chem. Sci.* **2018**, *9*, 7376.
[29] Y. Zhu, J. Carrete, Q.-L. Meng, Z. Huang, N. Mingo, P. Jiang, X. Bao, *J. Mater. Chem. A* **2018**, *6*, 7959.
[30] G. Tang, W. Wei, J. Zhang, Y. Li, X. Wang, G. Xu, C. Chang, Z. Wang, Y. Du, L. D. Zhao, *J. Am. Chem. Soc.* **2016**, *138*, 13647.
[31] R. Moshwan, L. Yang, J. Zou, Z.-G. Chen, *Adv. Funct. Mater.* **2017**, *27*, 1703278.
[32] Q. Zhang, B. Liao, Y. Lan, K. Lukas, W. Liu, K. Esfarjani, C. Opeil, D. Broido, G. Chen, Z. Ren, *Proc. Natl. Acad. Sci. USA* **2013**, *110*, 13261.
[33] G. Tan, L. D. Zhao, F. Shi, J. W. Doak, S. H. Lo, H. Sun, C. Wolverton, V. P. Dravid, C. Uher, M. G. Kanatzidis, *J. Am. Chem. Soc.* **2014**, *136*, 7006.
[34] R. Al Rahal Al Orabi, N. A. Mecholsky, J. Hwang, W. Kim, J.-S. Rhyee, D. Wee, M. Fornari, *Chem. Mater.* **2016**, *28*, 376.
[35] J. Tang, B. Gao, S. Lin, J. Li, Z. Chen, F. Xiong, W. Li, Y. Chen, Y. Pei, *Adv. Funct. Mater.* **2018**, *28*, 1803586.
[36] S. Johnsen, J. He, J. Androulakis, V. P. Dravid, I. Todorov, D. Y. Chung, M. G. Kanatzidis, *J. Am. Chem. Soc.* **2011**, *133*, 3460.
[37] L.-D. Zhao, J. He, C.-I. Wu, T. P. Hogan, X. Zhou, C. Uher, V. P. Dravid, M. G. Kanatzidis, *J. Am. Chem. Soc.* **2012**, *134*, 7902.
[38] Y. Zheng, S. Wang, W. Liu, Z. Yin, H. Li, X. Tang, C. Uher, *J. Phys. D: Appl. Phys.* **2014**, *47*, 115303.

[39] J. Androulakis, I. Todorov, J. He, D.-Y. Chung, V. Dravid, M. Kanatzidis, *J. Am. Chem. Soc.* **2011**, *133*, 10920.
[40] Q. Zhang, H. Wang, W. Liu, H. Wang, B. Yu, Q. Zhang, Z. Tian, G. Ni, S. Lee, K. Esfarjani, G. Chen, Z. Ren, *Energy Environ. Sci.* **2012**, *5*, 5246.
[41] Z. Chen, B. Ge, W. Li, S. Lin, J. Shen, Y. Chang, R. Hanus, G. J. Snyder, Y. Pei, *Nat. Commun.* **2017**, *8*, 13828.
[42] L. You, Y. Liu, X. Li, P. Nan, B. Ge, Y. Jiang, P. Luo, S. Pan, Y. Pei, W. Zhang, G. J. Snyder, J. Yang, J. Zhang, J. Luo, *Energy Environ. Sci.* **2018**, *11*, 1848.
[43] Z. Chen, Z. Jian, W. Li, Y. Chang, B. Ge, R. Hanus, J. Yang, Y. Chen, M. Huang, G. J. Snyder, Y. Pei, *Adv. Mater.* **2017**, *29*, 1606768.
[44] Y. Pei, A. D. LaLonde, N. A. Heinz, X. Shi, S. Iwanaga, H. Wang, L. Chen, G. J. Snyder, *Adv. Mater.* **2011**, *23*, 5674.
[45] P. Jood, M. Ohta, A. Yamamoto, M. G. Kanatzidis, *Joule* **2018**, *2*, 1339.
[46] X. Su, S. Hao, T. P. Bailey, S. Wang, I. Hadar, G. Tan, T.-B. Song, Q. Zhang, C. Uher, C. Wolverton, X. Tang, M. G. Kanatzidis, *Adv. Energy Mater.* **2018**, *8*, 1800659.
[47] H. J. Wu, L. D. Zhao, F. S. Zheng, D. Wu, Y. L. Pei, X. Tong, M. G. Kanatzidis, J. Q. He, *Nat. Commun.* **2014**, *5*, 5515.
[48] Y. He, T. Day, T. Zhang, H. Liu, X. Shi, L. Chen, G. J. Snyder, *Adv. Mater.* **2014**, *26*, 3974.
[49] L. Zhao, X. Wang, F. Y. Fei, J. Wang, Z. Cheng, S. Dou, J. Wang, G. J. Snyder, *J. Mater. Chem. A* **2015**, *3*, 9432.
[50] H. Liu, X. Shi, F. Xu, L. Zhang, W. Zhang, L. Chen, Q. Li, C. Uher, T. Day, G. J. Snyder, *Nat. Mater.* **2012**, *11*, 422.
[51] K. Zhao, A. B. Blichfeld, H. Chen, Q. Song, T. Zhang, C. Zhu, D. Ren, R. Hanus, P. Qiu, B. B. Iversen, F. Xu, G. J. Snyder, X. Shi, L. Chen, *Chem. Mater.* **2017**, *29*, 6367.
[52] B. Yu, W. Liu, S. Chen, H. Wang, H. Wang, G. Chen, Z. Ren, *Nano Energy* **2012**, *1*, 472.
[53] X. Su, F. Fu, Y. Yan, G. Zheng, T. Liang, Q. Zhang, X. Cheng, D. Yang, H. Chi, X. Tang, Q. Zhang, C. Uher, *Nat. Commun.* **2014**, *5*, 4908.
[54] K. Zhao, A. B. Blichfeld, E. Eikeland, P. Qiu, D. Ren, B. B. Iversen, X. Shi, L. Chen, *J. Mater. Chem. A* **2017**, *5*, 18148.
[55] L. L. Zhao, X. L. Wang, J. Y. Wang, Z. X. Cheng, S. X. Dou, J. Wang, L. Q. Liu, *Sci. Rep.* **2015**, *5*, 7671.
[56] R. Nunna, P. Qiu, M. Yin, H. Chen, R. Hanus, Q. Song, T. Zhang, M.-Y. Chou, M. T. Agne, J. He, G. J. Snyder, X. Shi, L. Chen, *Energy Environ. Sci.* **2017**, *10*, 1928.
[57] A. A. Olvera, N. A. Moroz, P. Sahoo, P. Ren, T. P. Bailey, A. A. Page, C. Uher, P. F. P. Poudeu, *Energy Environ. Sci.* **2017**, *10*, 1668.
[58] K. Zhao, H. Duan, N. Raghavendra, P. Qiu, Y. Zeng, W. Zhang, J. Yang, X. Shi, L. Chen, *Adv. Mater.* **2017**, *29*, 1701148.
[59] S. Ballikaya, H. Chi, J. R. Salvador, C. Uher, *J. Mater. Chem. A* **2013**, *1*, 12478.
[60] Y. He, T. Zhang, X. Shi, S.-H. Wei, L. Chen, *NPG Asia Mater.* **2015**, *7*, e210.
[61] M. M. Mallick, S. Vitta, *J. Appl. Phys.* **2017**, *122*, 024903.
[62] Y. Qiu, J. Ye, Y. Liu, X. Yang, *RSC Adv.* **2017**, *7*, 22558.
[63] Y. G. Asadov, L. V. Rustamova, G. B. Gasimov, K. M. Jafarov, A. G. Babajev, *Phase Transitions* **1992**, *38*, 247.
[64] R. Wu, Z. Li, Y. Li, L. You, P. Luo, J. Yang, J. Luo, *J. Materiomics* **2019**, *5*, 489.
[65] R. Graf, *J. Electrochem. Soc.* **1968**, *115*, 433.
[66] J. Linnera, A. J. Karttunen, *Phys. Rev. B* **2017**, *96*, 014304.
[67] A. Young, C. Schwartz, *J. Phys. Chem. Solids* **1969**, *30*, 249.
[68] S. P. Ong, W. D. Richards, A. Jain, G. Hautier, M. Kocher, S. Cholia, D. Gunter, V. L. Chevrier, K. A. Persson, G. Ceder, *Comput. Mater. Sci.* **2013**, *68*, 314.
[69] A. Jain, S. P. Ong, G. Hautier, W. Chen, W. D. Richards, S. Dacek, S. Cholia, D. Gunter, D. Skinner, G. Ceder, K. A. Persson, *APL Mater.* **2013**, *1*, 011002.
[70] D. Cahill, S. Watson, R. Pohl, *Phys. Rev. B* **1992**, *46*, 6131.
[71] G. Dennler, R. Chmielowski, S. Jacob, F. Capet, P. Roussel, S. Zastrow, K. Nielsch, I. Opahle, G. K. H. Madsen, *Adv. Energy Mater.* **2014**, *4*, 1301581.
[72] D. R. Brown, T. Day, T. Caillat, G. J. Snyder, *J. Electron. Mater.* **2013**, *42*, 2014.
[73] P. Qiu, M. T. Agne, Y. Liu, Y. Zhu, H. Chen, T. Mao, J. Yang, W. Zhang, S. M. Haile, W. G. Zeier, J. Janek, C. Uher, X. Shi, L. Chen, G. J. Snyder, *Nat. Commun.* **2018**, *9*, 2910.
[74] P. Qiu, T. Mao, Z. Huang, X. Xia, J. Liao, M. T. Agne, M. Gu, Q. Zhang, D. Ren, S. Bai, X. Shi, G. J. Snyder, L. Chen, *Joule* **2019**, *3*, 1538.
[75] J. P. Perdew, K. Burke, *Phys. Rev. Lett.* **1997**, *78*, 1396.
[76] J. P. Perdew, K. Burke, *Phys. Rev. Lett.* **1996**, *77*, 3865.
[77] P. E. Blöchl, *Phys. Rev. B* **1994**, *50*, 17953.
[78] G. Kresse, J. Furthmüller, *Phys. Rev. B* **1996**, *54*, 11169.
[79] A. van de Walle, P. Tiwary, M. de Jong, D. L. Olmsted, M. Asta, A. Dick, D. Shin, Y. Wang, L.-Q. Chen, Z.-K. Liu, *Calphad* **2013**, *42*, 13.